Applied Catalysis B: Environmental 142–143 (2013) 45–53

Contents lists available at SciVerse ScienceDirect

Applied Catalysis B: Environmental

journal homepage: www.elsevier.com/locate/apcatb

The new understanding on photocatalytic mechanism of visible-light response N—S codoped anatase TiO_2 by first-principles

Peng Zhou [a], Jiaguo Yu [a,*], Yuanxu Wang [b,**]

[a] State Key Laboratory of Advanced Technology for Materials Synthesis and Processing, Wuhan University of Technology, Wuhan 430070, People's Republic of China

[b] Institute for Computational Materials Science, School of Physics and Electronics, Henan University, Kaifeng 475004, People's Republic of China

ARTICLE INFO

Article history:
Received 7 March 2013
Received in revised form 23 April 2013
Accepted 28 April 2013
Available online 10 May 2013

Keywords:
TiO_2
N—S codoping
Visible light activity
Photocatalytic mechanism
First-principles

ABSTRACT

The geometry structure, formation energy and electronic property of N—S codoped anatase TiO_2 (NS—TiO_2) were investigated by the density functional theory (DFT) of first-principles. The result indicated that the O-poor growth condition is beneficial to the formation of NS—TiO_2 except the $N_{Ti}S_{Ti}$—TiO_2 with non-sensitivity to the atmosphere. The visible-light photocatalytic activity of NS—TiO_2 was influenced by many factors including the value of energy gap (E_g), the distribution of impurity level, the property of impurity level, the location of Fermi level and the energy in the edges of band gap. The impurity level localized in the top of valence band reduced the energy gap, leading to the absorption of visible light. Besides, the impurity level delocalized in the band gap reduced the critical energy of available photon, which further strengthened the absorption of visible light. Moreover, the bent impurity level was the efficient separation center of photogenerated electron and hole, while the flat impurity level was the combination center of photogenerated electron and hole. Further, the valence band and conduction band of NS—TiO_2 moved toward the low energy region (down shift), resulting in the stronger oxidizability of photogenerated hole in the top of valence band and weaker reducibility of photogenerated electron in the bottom of conduction band. This indicated that the dominant oxidant species during photocatalytic reaction for NS—TiO_2 was hole and $^{\bullet}OH$ radical instead of $^{\bullet}O_2^-$ ion.

1. Introduction

Since the photocatalytic H_2 production by splitting water on TiO_2 electrodes was reported in 1972 [1], semiconductor photocatalytic materials and technology have been widely investigated for the potential application in degradation of pollutant, photosynthesis of organic compounds and production of hydrogen [2–12]. Due to the chemical inertness, strong oxidizing power, nontoxicity, long-term stability and low cost, TiO_2 has been proven to be the most suitable photocatalytic material in hydrogen generation and environmental remediation among various oxide and nonoxide semiconductor photocatalysts [13,14]. However, with a large intrinsic band gap (3.2 eV for anatase and 3.0 eV for rutile), TiO_2 only can absorb the ultraviolet (UV) light which is a small portion of solar spectrum (containing about 4% ultraviolet light and 43% visible light) [15,16]. As a result, the effective utilization of visible light becomes a hot research topic. Many methods, including doping impurity atoms (B, C, N, F, P, S, Ni, etc.) [17–25] and sensitizing TiO_2 with organic dyes or narrow-gap semiconductor quantum dots (CdS, CdSe, InP, PbS, etc.) [26–31], have been developed to reduce the energy gap of TiO_2. As for the doping approaches, a large number of N-doped anatase TiO_2 (N—TiO_2) and S-doped anatase TiO_2 (S—TiO_2) have been synthesized, which shifts the absorption edge of TiO_2 into the visible region [32–40]. The corresponding theoretical study also has been performed to discuss the origination of absorption of visible light. Many literatures indicate that the band gap of doped TiO_2 is narrowed. But other literatures suggest that the impurity state in the band gap acts as the ladder for transferring electron, which reduces the maximum energy gap in the band gap [41–45]. Furthermore, the NS—TiO_2 is also prepared, indicating that NS—TiO_2 has higher visible-light photocatalytic activity than N—TiO_2 and S—TiO_2 [46–52]. But about the existing forms of N and S atom are often debated. Also, there is still no certain answer. Very recently, our group also synthesized the NS—TiO_2 [53], indicating that various defects induced by the impurity atoms exist in the doped TiO_2.

Herein, for the first time, we systematically investigate the geometry structure, formation energy and electronic property of NS—TiO_2. The stable NS—TiO_2 is determined by comparing the formation energy of doping process. The originations of enhanced visible-light photocatalytic activity are investigated by the value

* Corresponding author. Tel.: +86 27 87871029; fax: +86 27 87879468.
** Corresponding author. Tel.: +86 37 83881488; fax: +86 37 83881488.
E-mail addresses: jiaguoyu@yahoo.com (J. Yu), wangyx@henu.edu.cn (Y. Wang).

0926-3373/$ – see front matter © 2013 Elsevier B.V. All rights reserved.
http://dx.doi.org/10.1016/j.apcatb.2013.04.063

of energy gap, the distribution of the impurity state, the property of impurity state, the location of Fermi level and the energy value in the edges of band gap. This study will provide new insight into understanding the mechanism of enhanced visible-light photocatalytic activity for the NS—TiO_2 and designing new photocatalytic materials with required electronic property.

2. Computational details

All DFT calculations were performed with CASTEP package based on the plane-wave-pseudo-potential approach [54]. Considering the advantage of the generalized gradient approximation (GGA) in dealing with the electron gas of solid constituted of light atoms, the exchange-correlation function adopted the Perdew–Burke–Ernzerhof (PBE) of GGA [55,56]. The ultrasoft pseudo-potential was used to describe the interaction between valence electrons and the ionic core. The $2 \times 2 \times 1$ supercell (containing 16 Ti atoms and 32 O atoms, see Fig. 1) of anatase TiO_2 was simultaneously doped with one N atom and one S atom. The two impurity atoms were introduced into the supercell by the modes of N_O (N atom substituting lattice O atom), N_{Ti} (N atom substituting lattice Ti atom), N_i (N atom occupying the interstitial position), S_O (S atom substituting lattice O atom), S_{Ti} (S atom substituting lattice Ti atom) and S_i (S atom occupying the interstitial position), resulting in nine different kinds of N—S codoped anatase TiO_2 models. In addition, we kept the largest distance between the two impurity atoms as soon as possible to distribute the impurity atoms in the supercell. The doping concentrations (mole ratio) of the N and S atoms both changed from 2.08% (existing two substitutional atoms) to 2.00% (existing two interstitial atoms), similar to those obtained from some experiments [12,13]. The cutoff energy of 400 eV, the Monkhorst–Pack k-point mesh of $4 \times 4 \times 4$ and the self-consistent field of 5×10^{-5} eV/atom were used to perform geometry optimizations [57]. The optimized calculation was carried out until the energy, max force, max stress and max displacement were less than 2.0×10^{-5} eV/atom, 0.05 eV/Å, 0.1 GPa and 0.002 Å, respectively. Besides, the accuracy of the calculations was tested by improving the cutoff energy and the number of k point, the results of which showed that the energy and geometry structure almost did not changed. After the geometry optimization was finished, the band structure and projected density of state (PDOS) of NS—TiO_2 were calculated. Furthermore, to compare the electronic properties of NS—TiO_2 with those of single-doped TiO_2 (N—TiO_2 and S—TiO_2), the supercell models of N_O—TiO_2, N_{Ti}—TiO_2, N_i—TiO_2, S_O—TiO_2, S_{Ti}—TiO_2 and S_i—TiO_2 were also calculated.

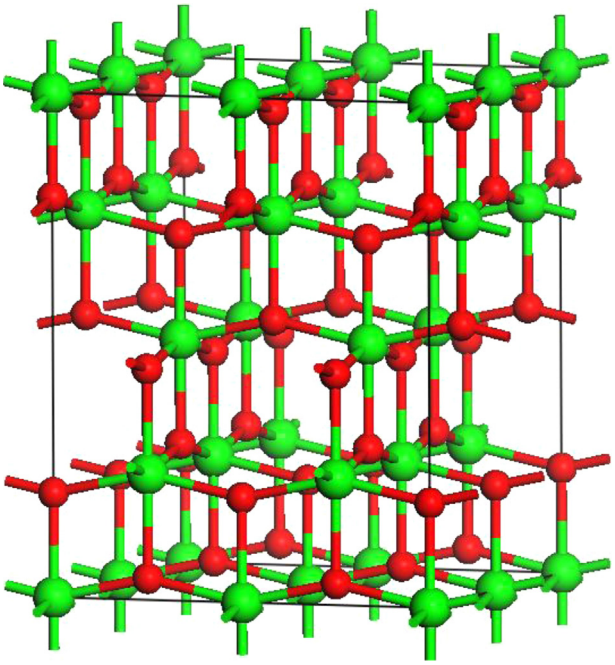

Fig. 1. The geometry structures for $2 \times 2 \times 1$ supercell of anatase TiO_2. The big green sphere represents Ti atom and the small red sphere represent O atom (For interpretation of the references to color in this figure legend, the reader is referred to the web version of the article.).

Table 1
Optimized cell parameters and bond lengths for N—S codoped anatase TiO_2.

No.	Doped TiO_2 [a]	Structure parameter (Å)				Bond length (Å)		
		a	*b*	*c*	N—O	N—Ti	S—O	S—Ti
(a)	N_OS_O	3.805	3.879	9.766		1.895_{eq}(2)[b] 1.917_{ax}		2.226_{eq}(2) 2.430_{ax}
(b)	$N_{Ti}S_{Ti}$	3.842	3.791	9.919	1.291_{eq} 1.282_{ax}		1.489_{eq} 1.523_{eq} 1.570_{ax}	
(c)	N_iS_i	3.871	3.844	9.715	1.458	2.035_{eq} 2.049_{eq} 2.063_{ax}	1.695 1.714	
(d)	N_OS_{Ti}	3.862	3.786	9.761		1.875_{eq} 1.902_{eq} 1.933_{ax}	1.504_{eq} 1.526_{eq} 1.566_{ax}	
(e)	$N_{Ti}S_O$	3.744	3.983	10.071	1.255_{eq} 1.284_{ax}			2.299_{eq} 2.339_{eq} 2.382_{ax}
(f)	N_OS_i	3.879	3.841	9.657		1.933_{eq} 1.922_{eq} 1.884_{ax}	1.696 1.709	
(g)	N_iS_O	3.813	3.806	10.155	1.319	2.057 2.060		2.236_{eq} 2.334_{eq} 2.362_{ax}
(h)	$N_{Ti}S_i$	3.915	3.821	9.962	1.221		1.638 1.680	
(i)	N_iS_{Ti}	3.851	3.818	9.842	1.464 1.449	2.247_{eq} 2.159_{ax}	1.595_{eq} 1.534_{eq} 1.616_{ax}	

[a] In pure anatase TiO_2: $a = b = 3.807$ Å, $c = 9.667$ Å, equatorial Ti—O = 1.947 Å and axial Ti—O = 2.005 Å.
[b] The number in the parentheses shows the number of bonds with same length.

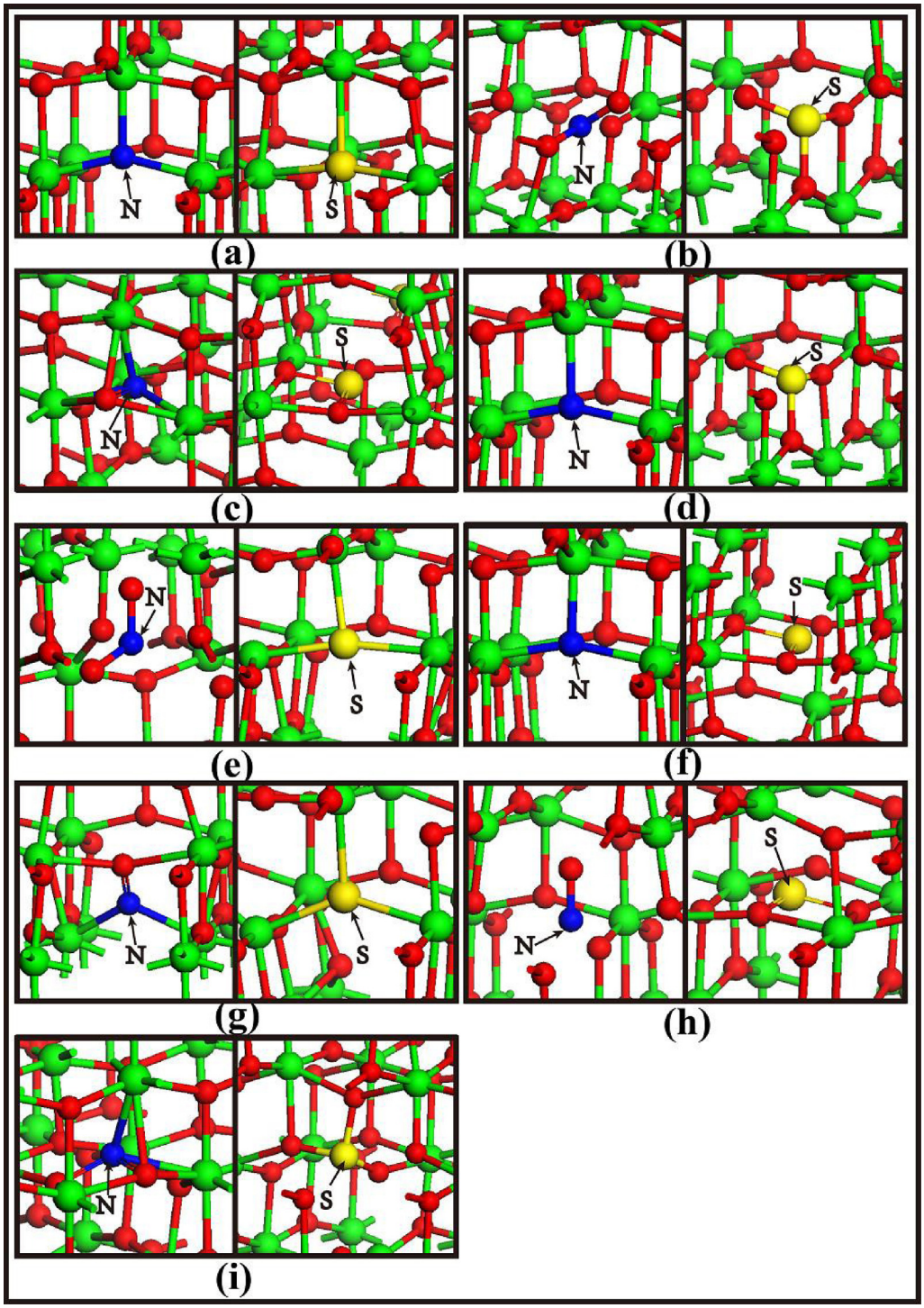

Fig. 2. The partial geometry structures for optimized N—S codoped anatase TiO_2 supercells: (a) N_OS_O—TiO_2, (b) $N_{Ti}S_{Ti}$—TiO_2, (c) N_iS_i—TiO_2, (d) N_OS_{Ti}—TiO_2, (e) $N_{Ti}S_O$—TiO_2, (f) N_OS_i—TiO_2, (g) N_iS_O—TiO_2, (h) $N_{Ti}S_i$—TiO_2, (i) N_iS_{Ti}—TiO_2. The green spheres stand for Ti atoms, the red spheres for O atoms, the blue spheres for N atoms, and the yellow spheres for S atoms (For interpretation of the references to color in this figure legend, the reader is referred to the web version of the article.).

3. Results and discussion

3.1. Optimized structures

In this work, the NS—TiO_2 was investigated. The partial geometry structures from the optimized supercells of NS—TiO_2 are shown in Fig. 2. It is clear that the N_O and S_O atoms in the doped TiO_2 (see Fig. 2a, d, e, f and g) all keep the initial coordination number of O atom, but the difference is that the lengths of Ti—S bonds (more than 2.2 Å, see Table 1) are larger than those of Ti—N bonds (less than 1.95 Å) and Ti—O bonds (1.947_{eq} and 2.005_{ax} Å) in pure anatase TiO_2. This is due to the larger radius of S atoms than those of N and O atoms. As a result, the structure parameters along with the direction of Ti—S bonds extend for a little. Because Ti—N_O bonds are shorter than Ti—O bonds in pure TiO_2, the structure parameters along with the direction of Ti—N_O bonds decrease. For the impurity atoms substitutional to Ti atoms, the N_{Ti} and S_{Ti} atoms cannot maintain same high coordination number with Ti atom, due to the

relatively simpler electronic orbits of N and S atoms than that of Ti atom. Thus the coordination numbers of the N_{Ti} and S_{Ti} atoms in the doped TiO_2 (see Fig. 2b, d, e, h and i) are smaller than that of Ti atom in pure TiO_2. Especially, the N_{Ti} atom in $N_{Ti}S_O$—TiO_2 forms the approximate NO_2 molecule (see Fig. 2e). However, the N_{Ti} atom in the $N_{Ti}S_i$—TiO_2 forms the approximate NO molecule (see Fig. 2h). This has been confirmed by the experiment [47]. But the S_{Ti} atoms in N_OS_{Ti}—TiO_2, $N_{Ti}S_{Ti}$—TiO_2 and N_iS_{Ti}—TiO_2 (see Fig. 2b, d and i) all are bonded to two equatorial O atoms and one axial O atom constituting the structures of SO_3 tetrahedron, which is confirmed by the XPS investigation [46]. Besides, the considerable modification of coordination number seriously changes the local lattice structure, resulting in the lattice distortion and the variation of cell parameter. For the impurity atoms in the interstitial position, the N_i atoms in the N_iS_i—TiO_2, N_iS_O—TiO_2 and N_iS_{Ti}—TiO_2 (see Fig. 2c, f and i) exhibit complex coordination modes. The N_i atoms are simultaneously bonded to the O and Ti atoms. However, the S_i atoms in N_iS_i—TiO_2, N_OS_i—TiO_2 and $N_{Ti}S_i$—TiO_2 (see Fig. 2c, f and h) all are only bonded to two adjacent O atoms. Though the introduced interstitial atoms form some new N_i—O (ranging from 1.319 to 1.464 Å) and S_i—O (ranging from 1.638 to 1.714 Å) bonds which are longer than the corresponding N_{Ti}—O (ranging from 1.221 to 1.291 Å) and S_{Ti}—O (ranging from 1.489 to 1.616 Å) bonds, the coordination numbers of most matrix atoms are not modified, implying little lattice deformation. Therefore, compared to the N_{Ti} and S_{Ti} atoms, the N_i and S_i atoms generates the smaller change in lattice structure. It should be noted that the coordination modes of N_{Ti} and N_i atoms vary with the location of S atom (S_O, S_{Ti} and S_i) though the N and S atoms are not directly bonded to each other, implying the indirect interaction existing between N and S atoms. But the coordination modes of S_O, S_{Ti} and S_i atoms are not influenced by the N atom, considered from the larger atom radius and weaker mobility of S atom than those of N atom.

3.2. Formation energies

The analysis on optimized geometry structure shows that the different doping ways generate different lattice distortions, which makes the supercells of NS—TiO_2 with various total energies. Therefore, to compare the relative feasibilities of doping ways above, the formation energies (E_{form}) of NS—TiO_2 supercells were investigated. The E_{form} is calculated by following formula:

$$E_{form} = E_{doped} - E_{pure} - \mu_N - \mu_S + x\mu_O + y\mu_{Ti} \quad (1)$$

where E_{doped} is the total energy of NS—TiO_2 supercell and E_{pure} is the total energy of the pure TiO_2 supercell [58,59]. μ_N, μ_S, μ_O and μ_{Ti} are the chemical potentials of N, S, O and Ti atoms, respectively. The coefficients x and y (equal to 0, 1 or 2) represent the numbers of O and Ti atoms substituted by impurity atoms, respectively. It should be mentioned that E_{form} is not fixed but depends on the growth condition. By adjusting the O_2 pressure, the growth condition can be changed from O-rich to Ti-rich (O-poor). The relationships between μ_O and the chemical potentials of N, S and Ti atoms are as follows:

$$2\mu_O + \mu_N = \mu(NO_2) \quad (2)$$

$$2\mu_O + \mu_S = \mu(SO_2) \quad (3)$$

$$2\mu_O + \mu_{Ti} = \mu(TiO_2) \quad (4)$$

Under O-rich growth condition, μ_O is determined by the ground-state energy of the O_2 molecule ($\mu_O = \mu(O_2)/2$). Thus the chemical potentials of N, S and Ti atoms can be obtained from the formulae (2)–(4), respectively. Under O-poor growth condition, μ_{Ti} is determined by the ground-state energy of bulk Ti ($\mu_{Ti} = \mu_{bulk}/n$, n is the number of Ti atom in the bulk Ti). According to the formula (4), μ_O is calculated. Then μ_N and μ_S can be obtained from the formulae (2) and (3), respectively. Considering that the calculated μ_O in O-rich growth condition are more 5 eV than that in O-poor growth condition, μ_O is transformed into the form of $\mu_O = \mu(O_2)/2 + \mu'_O$, where $\mu'_O = -5$ eV corresponds to O-poor growth condition and $\mu'_O = 0$ eV corresponds to the O-rich growth condition (condensation oxygen). According to the formulae (1)–(4), E_{form} are calculated from the following formula:

$$E_{form} = E_{doped} - E_{pure} - \mu(NO_2) - \mu(SO_2) + \times(2 + x/2 - y) \times \mu(O_2) + y\mu(TiO_2) + (4 + x - 2y) \times \mu'_O \quad (5)$$

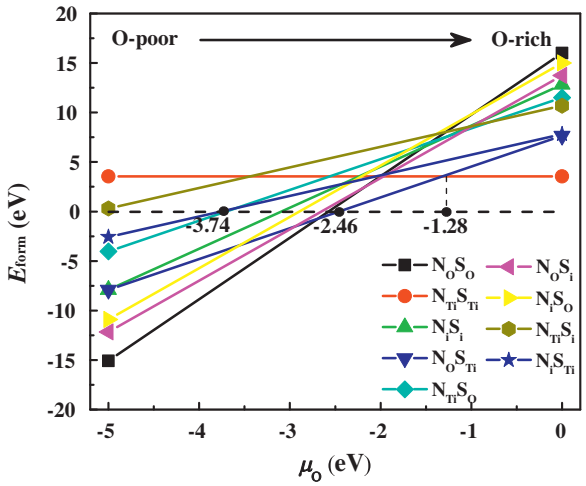

Fig. 3. Formation energies (eV) for the N—S codoped anatase TiO_2.

Consequently, the E_{form} of NS—TiO_2 can be regarded as the linear function of μ'_O. The μ'_O can range from −5 to 0 eV. Fig. 3 exhibits the functional relationship between E_{form} and μ'_O for the nine different kinds of NS—TiO_2. It can be clearly seen that the E_{form} of $N_{Ti}S_{Ti}$—TiO_2 does not change with μ'_O, while the E_{form} of other NS—TiO_2 increase with μ'_O rising. It is obvious that the $N_{Ti}S_{Ti}$—TiO_2 is not sensitive to the outside atmosphere. However, the O-poor condition supports the formation of other NS—TiO_2 (anaerobic NS—TiO_2). Especially, the N_OS_O—TiO_2 has the lowest E_{form} under the O-poor condition. Besides, the E_{form} of N_OS_i—TiO_2 and N_iS_O—TiO_2 are lower than −10 eV. This confirms that the N and S atoms prefer to substitute O atom or occupy the interstice of lattice under the O-poor condition. The previous analysis on geometry structure verifies that the N—Ti—O, N—O—Ti, S—Ti—O and S—O—Ti linkages exist in the N_OS_O—TiO_2, N_OS_i—TiO_2 and N_iS_O—TiO_2, which are consistent with many experiments [46,48,50,53]. As the μ'_O is below −3.74 eV, the E_{form} of anaerobic NS—TiO_2 except the $N_{Ti}S_{Ti}$—TiO_2 and $N_{Ti}S_i$—TiO_2 are lower than zero, indicating that the corresponding doping processes all are exothermic reactions. In contrast, the doping processes of the $N_{Ti}S_{Ti}$—TiO_2 and $N_{Ti}S_i$—TiO_2 with positive E_{form} require the extra energy supplied by environment, which is more difficult to perform. With the μ'_O moving forward higher chemical potential, the E_{form} of the anaerobic NS—TiO_2 gradually pass over zero point. As the μ'_O is bigger than −2.46 eV, the doping processes of all NS—TiO_2 with positive E_{form} become non-spontaneous reactions, implying that the O-rich condition inhibits the doping process of NS—TiO_2. But considering the relatively lower E_{form} of $N_{Ti}S_{Ti}$—TiO_2 and N_OS_{Ti}—TiO_2 under μ'_O from −2.46 to 0 eV, it is still possible to synthesize the $N_{Ti}S_{Ti}$—TiO_2 and N_OS_{Ti}—TiO_2 by controlling the O_2 pressure and supplying enough energy. The previous experiment indicated the NS—TiO_2 could be prepared by annealing in air (approximate O-rich condition), in which the structures of O—N—O and S—O—Ti linkage were detected by the XPS technology [47]. The

Table 2
The E_v, E_1, E_2, E_c, E_g and E_{max} for the pure and N—S codoped anatase TiO_2.

No.	Doped TiO_2	E_v (eV)	E_1 (eV)	E_2 (eV)	E_c (eV)	E_g (eV)	E_{max} (eV)
(a)	Pure	5.81	5.81	7.93	7.93	2.12	2.12
(b)	N_OS_O	4.54	4.54	6.06	6.06	1.52	1.52
(c)	$N_{Ti}S_{Ti}$	3.54	4.29	5.56	5.93	2.39	1.27
(d)	N_OS_{Ti}	3.86	4.70	6.15	6.15	2.29	1.45
(e)	N_OS_i	4.43	5.52	6.37	6.37	1.94	0.85
(f)	N_iS_O	3.90	5.31	6.41	6.41	2.51	1.10

result is quite consistent with the analysis on geometry structure (see Fig. 2b and d). Hence, to further investigate the photocatalytic activities of NS—TiO_2, the electronic properties of N_OS_O—TiO_2, $N_{Ti}S_{Ti}$—TiO_2, N_OS_{Ti}—TiO_2, N_OS_i—TiO_2 and N_iS_O—TiO_2 are discussed in the next section.

3.3. Electronic properties

To clarify the origination of enhanced visible-light photocatalytic activity of NS—TiO_2, the electronic properties of pure-TiO_2, N_OS_O—TiO_2, $N_{Ti}S_{Ti}$—TiO_2, N_OS_{Ti}—TiO_2, N_OS_i—TiO_2 and N_iS_O—TiO_2 are calculated by DFT. The calculated band structures and projected density of states (PDOS) of the pure and NS—TiO_2 are plotted in Fig. 4. Based on the calculated band structures, the E_v (the energy for the top of valence band), E_1 (the energy for the bottom of the maximum gap in band gap), E_2 (the energy for the top of the maximum gap in band gap), E_c (the energy for the bottom of conduction band), E_g (the energy for the band gap) and E_{max} (the energy for the maximum gap in band gap, $E_{max} = E_1 - E_2$) of the pure and NS—TiO_2 are listed in Table 2.

The calculated E_g of pure-TiO_2 is 2.12 eV, which is lower than the experimental value of 3.20 eV. The underestimation is originated from the known limitation of DFT. The conduction band of pure-TiO_2 (see Fig. 4a) is mainly constituted of Ti 3d states, while the valence band is composed of O 2p and Ti 3d states. For the N_OS_O—TiO_2 (see Fig. 4b), the conduction band still consists of the Ti 3d state, while the N_O 2p and S_O 3p states appear in the top of valence band. Thus the valence band extends forward the conduction band and the E_g is sharply decreased to 1.52 eV. Because of no impurity state in the band gap, the E_{max} is also 1.52 eV, which makes the absorption edge of N_OS_O—TiO_2 shift to the visible region. Different with those in the N_OS_O—TiO_2, the N_{Ti} 2s, N_{Ti} 2p, S_{Ti} 3s and S_{Ti} 3p states in the $N_{Ti}S_{Ti}$—TiO_2 (see Fig. 4c) are delocalized above the top of valence band. Especially, the N_{Ti} 2s and S_{Ti} 3s states appear in the same energy region with the N_{Ti} 2p and S_{Ti} 3p state, respectively, implying the hybridization of N_{Ti} 2s (S_{Ti} 3s) and N_{Ti} 2p (S_{Ti} 3p) states. Besides, a level of N_{Ti} 2p state is delocalized below the bottom of conduction band. As a result, the E_{max} (1.27 eV) of $N_{Ti}S_{Ti}$—TiO_2 becomes smaller than that of N_OS_O—TiO_2 though the E_g of $N_{Ti}S_{Ti}$—TiO_2 is increased to 2.39 eV, which greatly decreases the critical energy of photon required by transfering electron. Surprisingly, the distributing regulations of N_O 2p, S_{Ti} 3s and S_{Ti} 3p states in the N_OS_{Ti}—TiO_2 (see Fig. 4d) are similar to those of the N_O 2p state in N_OS_O—TiO_2 and S_{Ti} 3s and S_{Ti} 3p states in $N_{Ti}S_{Ti}$—TiO_2. This suggests that the N_O 2p state tend to be localized in the top of valence band, which leads to the extending of valence band. However, the hybridizing level of S_{Ti} 2s and S_{Ti} 2p states prefers to be delocalized above the valence band of N_OS_{Ti}—TiO_2, which is beneficial to the decrease of E_{max}. Thus compared to the $N_{Ti}S_{Ti}$—TiO_2, the E_g of N_OS_{Ti}—TiO_2 is reduced to 2.29 eV. But the E_{max} of N_OS_{Ti}—TiO_2 rises to 1.72 eV, mainly originating from no impurity state below the conduction band in the N_OS_{Ti}—TiO_2. Different with the impurity states in the N_OS_O—TiO_2, $N_{Ti}S_{Ti}$—TiO_2 and N_OS_{Ti}—TiO_2, the S_i 3p state in N_OS_i—TiO_2 (see Fig. 4e) and partial N_i 2p state in N_iS_O—TiO_2 (see Fig. 4f) go deep into the band gap. As a result, the E_{max} of N_OS_i—TiO_2 and N_iS_O—TiO_2 are significantly decreased to 0.85 eV and 1.10 eV, respectively. Because of the N 2p and S 3s states localized in the top of valence band, the E_g of N_OS_i—TiO_2 is also reduced by 0.18 eV. In contrast, the E_g of N_iS_O—TiO_2 is decreased to 2.51 eV, mostly considered from the delocalization of N 2p and S 3p states. Therefore, the discussed impurity states all contributes to the red shift of NS—TiO_2.

But according to many previous investigations, the visible-light photocatalytic activity is not only determined by the quantity of available photons, but also influenced by the quantum efficiency. The visible-light absorption of NS—TiO_2 only increases the quantity of available photons, but is not directly related to the quantum efficiency. However, it is much known that the recombination of photogenerated electron and hole easily occurs during the photocatalytic reaction and becomes the largest barrier for enhancing quantum efficiency. For the doped photocatalyst, many literatures discuss the impurity state delocalized in band gap as the recombination center of photogenerated electron and hole [60]. In contrast, other investigations also suggest that the impurity level in band gap is the separation center of photogenerated electron and hole [61,62]. But in fact, whether the impurity level is beneficial to enhancing quantum efficiency or not largely depends on the property of impurity level. During the photocatalytic reaction, the electron in the impurity level moves to the conduction band by capturing a photon with enough energy. Meanwhile a hole is left in the impurity level. Then the electron from the valence band can jump to the impurity level by capturing another appropriate photon, which means that the hole in the impurity level is eliminated and new hole forms in the top of valence band. As a result, the impurity level does not change, while an electron and a hole are generated in the valence band and conduction band, respectively, indicating the separation of photogenerated electron and hole. But this process is mainly determined by the mobility of photogenerated electron and hole, which can be indirectly characterized by the efficient masses (absolute value) of electron and hole. The smaller the efficient mass, the better the mobility. On the contrary, the larger efficient mass results in the worse mobility. The efficient masses of electron and hole are determined by the following formula:

$$m^* = \pm \frac{h/2\pi^2}{(d^2E/dk^2)^2} \quad (6)$$

where m^* is the efficient mass, h is the Planck constant, k is the wave vector and E is the energy of k. The positive and negative signs correspond to the electron and hole, respectively. It is clear that the electron and hole in the flat level with constant gradient have higher efficient masses, and contrarily those in bent level with variable gradient have lower efficient masses. In Fig. 4, compared to the levels of impurity states in other NS—TiO_2, the hybridizing levels of S 3s and S 3p states in N_OS_{Ti}—TiO_2 and N_OS_{Ti}—TiO_2 show the more obvious bend, indicating that the present levels are the efficient separation center of photogenerated electron and hole. However, the levels of N 2p state in $N_{Ti}S_{Ti}$—TiO_2 and N_iS_O—TiO_2 are approximate to straight line, corresponding to the recombination center of photogenerated electron and hole. Therefore, the shape and location of level of impurity state both are closely related to the photocatalytic activity of NS—TiO_2.

Furthermore, according to the E_v and E_c in Table 2, it can be clearly seen that the valence and conduction bands of NS—TiO_2 both move down to the lower energy region. The E_v and E_c are decreased by more than 1.20 eV. It is easy to understand that the electron from donor (such as organic pollutant and OH^-) is easier to jump to the lower energy level and combine with the photogenerated hole. Similarly, the photogenerated electron in the conduction band is also easier to shift to the empty energy level of acceptor (such as O_2). In other words, the photogenerated hole in the lower energy level and the photogenerated electron in the higher energy level have

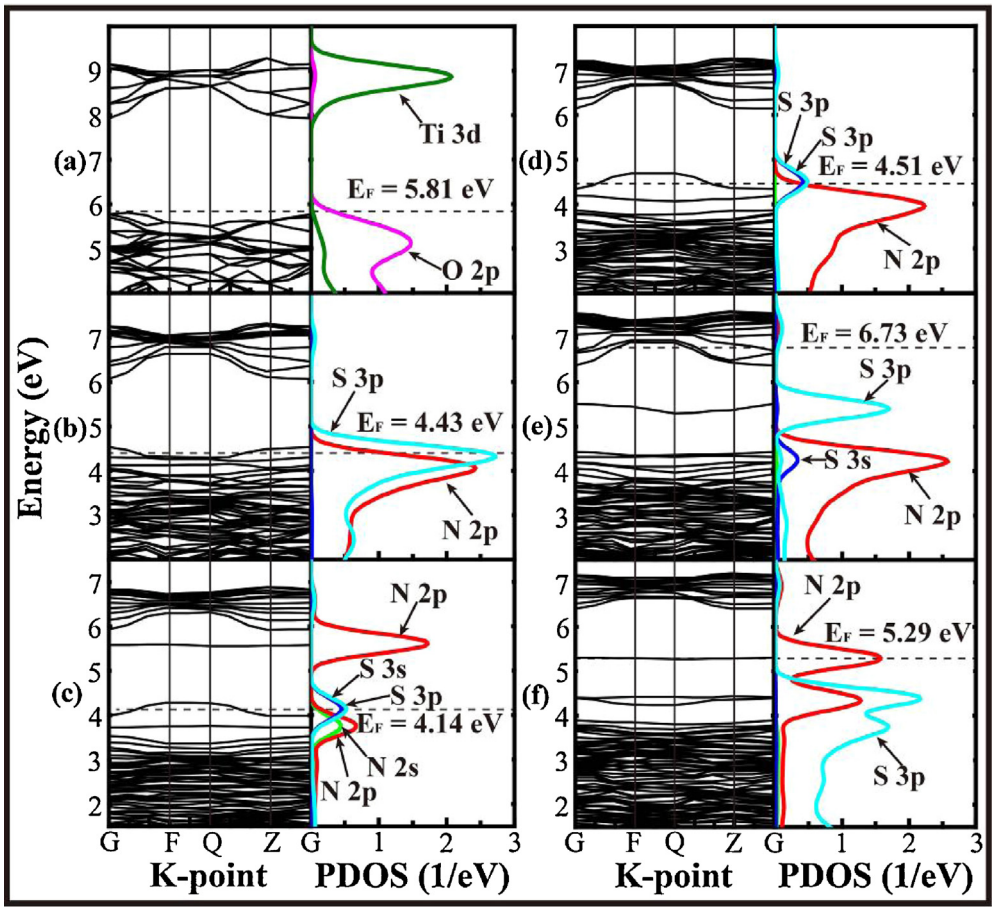

Fig. 4. Band structures and projected density of state (PDOS) plots for pure and N—S codoped TiO_2: (a) pure-TiO_2, (b) N_OS_O—TiO_2, (c) $N_{Ti}S_{Ti}$—TiO_2, (d) N_OS_{Ti}—TiO_2, (e) N_OS_i—TiO_2 and (f) N_iS_O—TiO_2. To compare relative energies of band structures and PDOS for different N—S codoped TiO_2, all energies are raised by the corresponding E_F. The dashed lines stand for the Fermi level. The magenta lines represent the PDOS of O 2p, olive for Ti 3d, green for N 2s, red for N 2p, blue for S 3s and cyan for S 3p (For interpretation of the references to color in this figure legend, the reader is referred to the web version of the article.).

the stronger oxidizability and reducibility, respectively. Therefore, the oxidizability of photogenerated hole in the top of valence band is enhanced and the reducibility of photogenerated electron in the bottom of conduction band is weakened in the NS—TiO_2. According to many previous investigations on the mechanism of photocatalytic degradation, it is widely confirmed that the O_2 on the surface of TiO_2 can be reduced into $^{\bullet}O_2^-$ ion by capturing a photogenerated electron from the conduction band. In contrast, the hydroxyl group (—OH) on the surface of TiO_2 can be oxidized into $^{\bullet}OH$ radical by capturing a photogenerated hole from the valence band. In addition, the photogenerated hole also can be directly captured by the organic pollutant. These $^{\bullet}O_2^-$ ion, $^{\bullet}OH$ radical and hole all are crucial oxidants in the degradation of organic pollutant. As a result, the NS—TiO_2 prefers to generate more $^{\bullet}OH$ radicals, rather than $^{\bullet}O_2^-$ ions. Moreover, for different organic pollutants and photocatalysts, the contributions of $^{\bullet}O_2^-$ ion, $^{\bullet}OH$ radical and hole are also different. Our recent study on the degradation of Rhodamine B (RhB) with B-C codoped anatase TiO_2 indicates that the $^{\bullet}OH$ radical plays the domain role in the photocatalytic reaction. This is because the location of the valence band edges (E_v) of B-C codoped anatase TiO_2 is lower than the normal potential of the $OH^-/^{\bullet}OH$ couple [61–63]. However, another investigation on the degradation of methyl orange (MO) with BiOI confirms that the hole is the main oxidant. This is due to the valence band edges (E_v) of BiOI is higher than the $OH^-/^{\bullet}OH$ couple potential [64]. Hence, the energy values in the top of valence band and bottom of conduction band have a significant influence on the mechanism of photocatalytic reaction.

Considering the variation of Fermi levels in the NS—TiO_2, the further investigation is done. The E_F in pure anatase TiO_2 is 5.81 eV, while the E_F in NS—TiO_2 ranges from 4.14 ($N_{Ti}S_{Ti}$—TiO_2) to 6.73 eV (N_OS_i—TiO_2). Besides, because of the moving of valence band and conduction band, the distance between the Fermi level and the valence band (conduction band) also exhibits different change. The shift of Fermi level implies the redistribution of charges after doping N and S atoms into the lattice of TiO_2. To investigate the origination of shift of Fermi level, the Mulliken populations of NS—TiO_2 are calculated (see Table 3). In pure anatase TiO_2, the Mulliken populations of O and Ti atoms are −0.67 and 1.33, respectively. Besides, as a typical semiconductor, the Fermi level of pure-TiO_2 is in the top of valence band. But in the N_OS_O—TiO_2, the Mulliken populations of Ti atoms bonded to N_O and S_O atoms are lower than 1.33 because

Table 3
The E_v, E_1, E_2, E_c, E_g and E_{max} for the N- and S-doped anatase TiO_2.

No.	Doped TiO_2	E_v (eV)	E_1 (eV)	E_2 (eV)	E_c (eV)	E_g (eV)	E_{max} (eV)
(a)	N_O	4.46	4.46	6.12	6.12	1.66	1.66
(b)	N_{Ti}	3.65	3.65	5.48	5.94	2.29	1.83
(c)	N_i	4.09	4.09	5.83	6.25	2.16	1.74
(d)	S_O	5.26	5.73	7.16	7.16	1.90	1.43
(e)	S_{Ti}	4.92	5.90	7.15	7.15	2.23	1.25
(f)	S_i	4.16	4.67	5.55	6.37	2.21	0.88

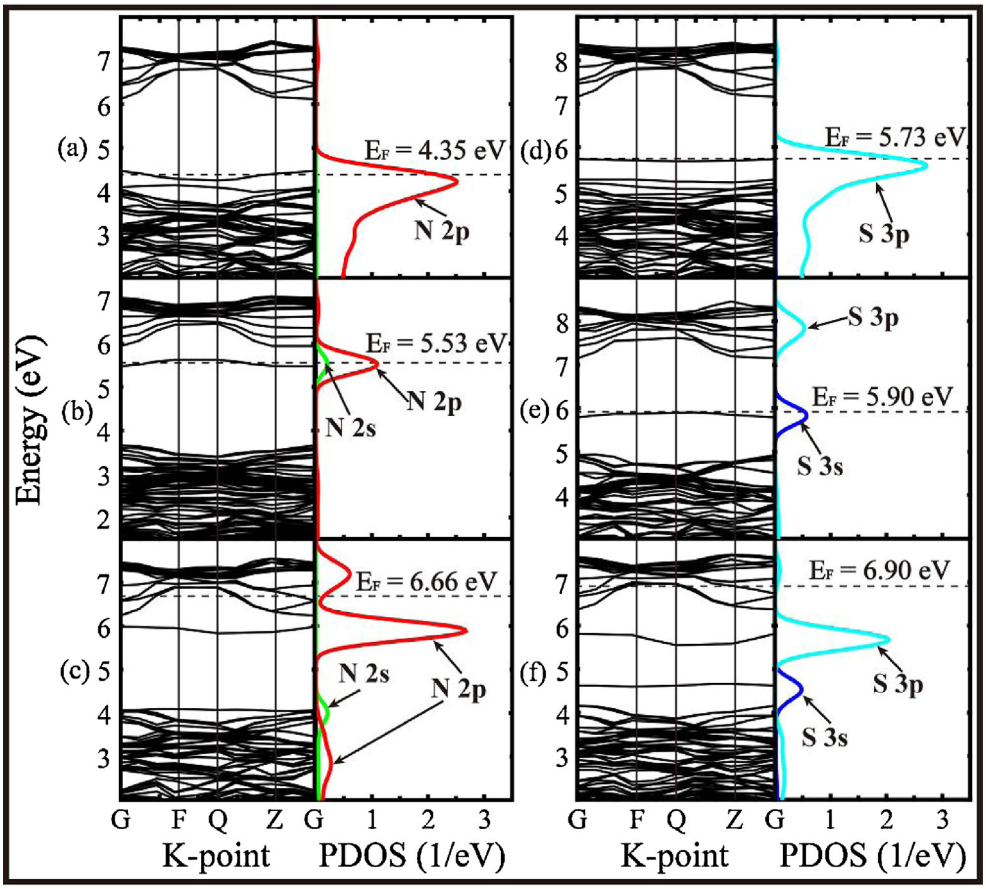

Fig. 5. Band structures and PDOS plots for N- and S-doped anatase TiO_2: (a) N_O—TiO_2, (b) N_{Ti}—TiO_2, (c) N_i—TiO_2, (d) S_O—TiO_2, (e) S_{Ti}—TiO_2 and (f) S_i—TiO_2. Other refers to Fig. 4.

the electronegativity of N and S atoms is smaller than that of O atom. However, the Mulliken population of N_O atom is larger than that of O atom in pure-TiO_2, due to the fact that the N_O—Ti bond is shorter than O—Ti bond (see Table 1). As a result, the adjacent Ti atoms prefer to be close to the N_O atom rather than O atom. Meanwhile, the interaction between O and Ti atoms is also weakened. This explains why the Mulliken populations of Ti atoms bonded to N_O atom are decreased, while the Mulliken population of N_O atom rises. As for S_O atom, the Mulliken population of S_O atom is only −0.21 because of its weak electronegativity. This is well consistent with the fact that the Fermi level is nearly above the N_O 2p state and in the middle of S_O 3p state (see Fig. 4b), indicating that the level of N_O 2p state is filled with electrons and that of S_O 3p state is half filled. However, the Fermi levels in the $N_{Ti}S_{Ti}$—TiO_2 and N_OS_{Ti}—TiO_2 both are delocalized in the band gap, approaching to the middle of hybridizing levels of S_{Ti} 3s and S_{Ti} 3p states. This indicates that the hybridizing levels of S_{Ti} 3s and S_{Ti} 3p states are also half filled. The previous analysis on the efficient mass indicates that the

Table 4
Mulliken populations on the impurity and adjacent matrix atoms in the supercells of N—S codoped anatase TiO_2.

Doped TiO_2 [a]	N population	S population	O population		Ti population	
			Bonded to N	Bonded to S	Bonded to N	Bonded to S
N_OS_O	−0.69	−0.21			1.28_{eq}(2)[b] 1.30_{ax}	1.18_{eq}(2) 1.25_{ax}
$N_{Ti}S_{Ti}$	0.25	1.79	-0.39_{eq} -0.40_{ax}	-0.80_{eq} -0.82_{eq} -0.76_{ax}		
N_OS_{Ti}	−0.69	1.77		-0.80_{eq} -0.82_{eq} -0.77_{ax}	1.27_{eq} 1.28_{eq} 1.28_{ax}	
N_OS_i	−0.69	0.67		−0.71 −0.73	1.25_{eq} 1.27_{eq} 1.26_{ax}	
N_iS_O	−0.25	−0.37	−0.37		1.25 1.26	1.13_{eq} 1.18_{eq} 1.18_{ax}

[a] In the pure anatase TiO_2: O population = −0.67, Ti population = 1.33.
[b] The numbers in the parentheses describes the quantity of atoms with same Mulliken population.

hybridizing levels of S_{Ti} 3s and S_{Ti} 3p states are the efficient separation center of photogenerated electron and hole. As a result, not only can the electrons in the present levels directly jump to the conduction bands, but also the electrons in the valence bands can jump to the present levels. But the hybridizing level of N_{Ti} 2s and N_{Ti} 2p states in $N_{Ti}S_{Ti}$—TiO_2 are filled, owing to the Mulliken population (0.25) of N_{Ti} atom smaller than that (1.79) of S_{Ti} atom. Similar to that in N_OS_O—TiO_2, the level of N_O 2p state in N_OS_{Ti}—TiO_2 is also filled. However, in N_OS_i—TiO_2, the Fermi level enters the bottom of conduction band, indicating that the N_OS_i—TiO_2 has the metal-like electroconductivity and the Ti^{3+} ion exists in the present TiO_2. This is due to the fact that the S_i atom is bonded to O atoms (see Fig. 2i) and shows the positive Mulliken population (0.67), which weakens adjacent O—Ti bonds and decreases the quantity of electrons transferring from Ti atoms to O atoms. Therefore, compared to those in pure-TiO_2, the more levels of Ti 3d state in N_OS_i—TiO_2 are occupied. The modified electroconductivity of N_OS_i—TiO_2 are in favor of the transferring of photogenerated electron, which improves the separating rate of photogenerated electron and hole. Though in N_iS_O—TiO_2 the interstitial atom (N) is also introduced, the N_i atom is simultaneously bonded to Ti and O atom and shows negative Mulliken population (−0.25). Besides, the Mulliken population of O atom bonded to N_i atom is decreased to −0.37. Thus the Fermi level is delocalized in the level of N_i 2p state, indicating that the present level is half filled. However, the previous analysis shows that the efficient mass of electron in the present level is greater than that in other levels. Therefore the electron in present level cannot easily transfer to the conduction band. Besides, the electron from the valence band or other impurity levels can be trapped in the present level, which inhibits the transferring of electron.

Another phenomenon should be noted that the distributions of S_O 3p states in the N_OS_O—TiO_2 (see Fig. 4b) and N_iS_O—TiO_2 (see Fig. 4f) are different though the S atoms both are doped in the positions of O atoms. Hence, the impurity level of S atom is influenced by N atom, indicating that the band structure of NS—TiO_2 is not mechanical mixture of the band structures of N—TiO_2 and S—TiO_2. Thus, to explore the interaction between N and S atoms, the N—TiO_2 (N_O—TiO_2, N_{Ti}—TiO_2 and N_i—TiO_2) and S-doped TiO_2 (S_O—TiO_2, S_{Ti}—TiO_2 and S_i—TiO_2) are also investigated. The calculated band structure and PDOS are shown in Fig. 5. In addition, the E_v, E_1, E_2, E_c, E_g and E_{max} are also calculated (see Table 4). It can be seen clearly that the level of N_O 2p state in the N_O—TiO_2 (see Fig. 5a) and the level of S_O 3p state in the S_O—TiO_2 (see Fig. 5d) both tend to be delocalized above the valence band, different with those in the N_OS_O—TiO_2. As a result, the E_g of N_O—TiO_2 (1.66 eV) and S_O—TiO_2 (1.90 eV) are larger than that of N_OS_O—TiO_2. Besides, the Fermi levels are delocalized in the levels of N 2p and S 3p states, indicating that the levels of N 2p and S 3p states are mostly filled. In the N_{Ti}—TiO_2 (see Fig. 5b), the N 2s state hybridizes with N 2p state, similar to that in the $N_{Ti}S_{Ti}$—TiO_2. However, the hybridizing level of N_{Ti} 2s and N_{Ti} 2p states is close to the bottom of conduction band. Besides, the single N_{Ti} 2p state is not found in the band gap. In S_{Ti}—TiO_2 (see Fig. 5e), the S 3s and S 3p states are in different energy region. Especially, the S 3p state is localized in the conduction band. As a result, though the E_g of N_{Ti}—TiO_2 (2.29 eV) and S_{Ti}—TiO_2 (2.23 eV) are larger than that (2.12 eV) of pure-TiO_2, the E_{max} of N_{Ti}—TiO_2 (1.83 eV) and S_{Ti}—TiO_2 (1.25 eV) are smaller than 2.12 eV because of the delocalized levels. In the N_i—TiO_2 (see Fig. 5c) and S_i—TiO_2 (see Fig. 5f), the N_i 2p, S_i 3s and S_i 3p states are mainly delocalized in the band gap, while the N_i 2s state in N_i—TiO_2 is localized in the top of valence band. This results in that the E_g of N_i—TiO_2 (2.16 eV) and S_i—TiO_2 (2.21 eV) is slightly larger than that of pure-TiO_2 (2.12 eV), but the E_{max} of N_i—TiO_2 and S_i—TiO_2 are decreased to 1.74 and 0.88 eV, respectively. In addition, the Fermi levels of N_i—TiO_2 and S_i—TiO_2 both enter the conduction bands. Though in the N_iS_O—TiO_2 the Fermi level is also in the conduction band, the Fermi level in the N_OS_i—TiO_2 is only close to the middle of band gap, implying that the behavior of N_i atom is changed by S_O atom. Meanwhile, the S_O atom is also influenced by the N_i atom. Hence, the synergistic effects of N and S atoms make the NS—TiO_2 exhibit different electronic properties with those of N—TiO_2 and S—TiO_2. But the NS—TiO_2 also inherits partial electronic property of N—TiO_2 and S—TiO_2. This is be beneficial to synthesizing the NS—TiO_2 with expected electronic property.

4. Conclusions

The visible-light photocatalytic activity of NS—TiO_2 is studied by the first-principles. The NS—TiO_2 except $N_{Ti}S_{Ti}$—TiO_2 is the anaerobic doped system, which enjoys the O-poor growth condition. In the O-poor condition, the N_OS_O—TiO_2, N_OS_i—TiO_2 and N_iS_O—TiO_2 are the most stable doped system. However, with increasing the μ_O, the N_OS_{Ti}—TiO_2 and $N_{Ti}S_{Ti}$—TiO_2 successively become the most stable doped system. But the doping processes of N_OS_{Ti}—TiO_2 and $N_{Ti}S_{Ti}$—TiO_2 require extra energy. The photocatalytic activities of N_OS_O—TiO_2, $N_{Ti}S_{Ti}$—TiO_2, N_OS_{Ti}—TiO_2, N_OS_i—TiO_2 and N_iS_O—TiO_2 are determined not only by the values of energy gaps (E_g) and distributions of impurity states, but also depend on the properties of impurity states and the locations of Fermi levels. The impurity state localized in the valence band reduces the E_g and that delocalized in the band gap decreases the E_{max}, which both enhance the absorptions of visible light. But the separating efficiency of photogenerated electron and hole is controlled by the property of impurity level. In the $N_{Ti}S_{Ti}$—TiO_2 and N_OS_{Ti}—TiO_2, the hybridizing levels of S_{Ti} 3s and S_{Ti} 3p states are the effective separation center of photogenerated electron and hole, in which the photogenerated electron and hole have smaller efficient masses. In contrast, the level of N_{Ti} 2p state (close to the conduction band) in $N_{Ti}S_{Ti}$—TiO_2 and level of N_i 2p state (close to the middle of band gap) in N_iS_O—TiO_2 easily become the combination or trap center of photogenerated electron and hole. The N_OS_i—TiO_2 with Fermi level in the conduction band shows the best electroconductivity, which improves the ability of transferring electron. Furthermore, the valence band and conduction band of NS—TiO_2 move toward the lower energy region compared to those of pure-TiO_2, which enhances the oxidizability of photogenerated hole in the top of valence band but weakens the reducibility of photogenerated electron in the bottom of conduction band. This contributes to forming more $^{\bullet}OH$ radical than $^{\bullet}O_2^-$ ion during the photocatalytic reaction. In addition, the NS—TiO_2 not only exhibits many same electronic properties with N—TiO_2 and S—TiO_2, but also produces many new electronic properties, implying that the electronic property of NS—TiO_2 does not mechanically consist of those of N—TiO_2 and S—TiO_2. This investigation will provide some new insights into designing and synthesizing the codoped or multidoped TiO_2 system with expected electronic property by adjusting the growth condition.

Acknowledgements

This work was partially supported by the 973 program (2013CB632402), 863 Program (2012AA062701), NSFC (51072154, 21177100 and 51272199) and Natural Science Foundation of Hubei Province (2010CDA078). Also, this work was financially supported by the Fundamental Research Funds for the Central Universities and Self-determined and Innovative Research Funds (2013-ZD-1) of SKLWUT.

References

[1] A. Fujishima, K. Honda, Nature 238 (1972) 37.
[2] Y. Xu, M.A.A. Schoonen, American Mineralogist 85 (2000) 543.

[3] Q.J. Xiang, J.G. Yu, M. Jaroniec, Chemical Society Reviews 41 (2012) 782.
[4] M. Anpo, H. Yamashita, Y. Ishihashi, Y. Fujii, M. Honda, Journal of Physical Chemistry 101 (1997) 2632.
[5] P. Madhusudan, J.R. Ran, J. Zhang, J.G. Yu, G. Liu, Applied Catalysis B 110 (2011) 286.
[6] X.X. Yu, S.W. Liu, J.G. Yu, Applied Catalysis B 104 (2011) 12.
[7] W.G. Wang, J.G. Yu, Q.J. Xiang, B. Cheng, Applied Catalysis B 119–120 (2012) 109.
[8] T. Inoue, A. Fujishima, S. Konishi, K. Honda, Nature 277 (1979) 637.
[9] I. Lauermann, D. Meissner, R. Memming, Journal of Electroanalytical Chemistry 228 (1987) 45.
[10] J. Zhang, J.G. Yu, Y.M. Zhang, Q. Li, J.R. Gong, Nano Letters 11 (2011) 4774.
[11] Q.J. Xiang, J.G. Yu, M. Jaroniec, Journal of the American Ceramic Society 134 (2012) 6575.
[12] J. Zhang, J.G. Yu, M. Jaroniec, J.R. Gong, Nano Letters 12 (2012) 4584.
[13] S.W. Liu, J.G. Yu, M. Jaroniec, Journal of the American Ceramic Society 132 (2010) 11914.
[14] J.G. Yu, Y.R. Su, B. Cheng, Advanced Functional Materials 17 (2007) 1984.
[15] J.G. Yu, G.P. Dai, B.B. Huang, Journal of Physical Chemistry C 113 (2009) 16394.
[16] Q.J. Xiang, J.G. Yu, W.G. Wang, M. Jaroniec, Chemical Communications 47 (2011) 6906.
[17] X.N. Lu, B.Z. Tian, F. Chen, J.L. Zhang, Thin Solid Films 519 (2010) 111.
[18] Y. Park, W. Kim, H. Park, T. Tachikawa, T. Majima, W. Choi, Applied Catalysis B 91 (2009) 355.
[19] R. Asahi, T. Morikawa, T. Ohwaki, K. Aoki, Y. Taga, Science 293 (2001) 269.
[20] J.C. Yu, J.G. Yu, W.K. Ho, Z.T. Jiang, L.Z. Zhang, Chemistry of Materials 14 (2002) 3808.
[21] S.W. Liu, J.G. Yu, W.G. Wang, Physical Chemistry Chemical Physics 12 (2010) 12308.
[22] G.D. Yang, Z.F. Yan, T.C. Xiao, Applied Surface Science 258 (2012) 4016.
[23] M. Sathish, B. Viswanathan, R.P. Viswanath, C.S. Gopinath, Chemistry of Materials 17 (2005) 6349.
[24] F.F. Li, Y.S. Jiang, M.S. Xia, M.M. Sun, B. Xue, D.R. Liu, X.G. Zhang, Journal of Physical Chemistry C 113 (2009) 18134.
[25] X.H. Tang, D.Y. Li, Journal of Physical Chemistry C 112 (2008) 5405.
[26] R. Plass, S. Pelet, J. Krueger, M. Gratzel, U. Bach, Journal of Physical Chemistry B 106 (2002) 7578.
[27] S.G. Hickey, D.J. Riley, E.J. Tull, Journal of Physical Chemistry B 104 (2000) 7623.
[28] I. Robel, M. Kuno, P.V. Kamat, Journal of the American Ceramic Society 129 (2007) 4136.
[29] I. Robel, V. Subramanian, M. Kuno, P.V. Kamat, Journal of the American Ceramic Society 128 (2006) 2385.
[30] W.T. Sun, Y. Yu, H.Y. Pan, X.F. Gao, Q. Chen, L.M. Peng, Journal of the American Ceramic Society 130 (2008) 1124.
[31] L.F. Qi, J.G. Yu, M. Jaroniec, Physical Chemistry Chemical Physics 13 (2011) 8915.
[32] Y. Wang, C. Feng, M. Zhang, J.J. Yang, Z.J. Zhang, Applied Catalysis B 100 (2010) 84.
[33] G. Barolo, S. Livraghi, M. Chiesa, M.C. Paganini, E. Giamello, Journal of Physical Chemistry C 116 (2012) 20887.
[34] D.D. Camillo, F. Ruggieri, S. Santucci, L. Lozz, Journal of Physical Chemistry C 116 (2012) 18427.
[35] J. Wang, D.N. Tafen, J.P. Lewis, Z.L. Hong, A. Manivannan, M. Zhi, M. Li, N.Q. Wu, Journal of the American Ceramic Society 131 (2009) 12290.
[36] S.H. Nam, T.K. Kim, J.H. Boo, Catalysis Today 185 (2012) 259.
[37] H.X. Li, X.Y. Zhang, Y.N. Huo, J. Zhu, Environmental Science and Technology 41 (2007) 4410.
[38] Y. Cong, J.L. Zhang, F. Chen, M. Anpo, Journal of Physical Chemistry C 111 (2007) 6976.
[39] T. Tachikawa, Y. Takai, S. Tojo, M. Fujitsuka, H. Irie, K. Hashimoto, T. Majima, Journal of Physical Chemistry B 110 (2006) 13158.
[40] X.B. Chen, C. Burda, Journal of the American Ceramic Society 130 (2008) 5018.
[41] F.H. Tian, C.B. Liu, Journal of Physical Chemistry B 110 (2006) 17866.
[42] Z.S. Lin, A. Orlov, R.M. Lambert, M.C. Payne, Journal of Physical Chemistry B 109 (2005) 20948.
[43] Y. Cui, H. Du, L.S. Wen, Solid State Communications 149 (2009) 634.
[44] K.S. Yang, Y. Dai, B.B. Huang, Journal of Physical Chemistry C 111 (2007) 12086.
[45] K.S. Yang, Y. Dai, B.B. Huang, Journal of Physical Chemistry C 111 (2007) 18985.
[46] J.A. Rengifo-Herrera, K. Pierzchała, A. Sienkiewicz, L. Forro, J. Kiwi, C. Pulgarin, Applied Catalysis B 88 (2009) 398.
[47] J.A. Rengifo-Herrera, E. Mielczarski, J. Mielczarski, N.C. Castillo, J. Kiwi, C. Pulgarin, Applied Catalysis B 84 (2008) 448.
[48] K.M. Parida, N. Sahu, A.K. Tripathi, V.S. Kamble, Environmental Science and Technology 44 (2010) 4155.
[49] M. Ksibi, S. Rossignol, J.M. Tatibouët, C. Trapalis, Materials Letters 62 (2008) 4204.
[50] J.A. Rengifo-Herrera, C. Pulgarin, Solar Energy 84 (2010) 37.
[51] G.T. Yan, M. Zhang, J. Hou, J.J. Yang, Materials Chemistry and Physics 129 (2011) 553.
[52] M. Behpour, V. Atouf, Applied Surface Science 258 (2012) 6595.
[53] Q.J. Xiang, J.G. Yu, M. Jaroniec, Physical Chemistry Chemical Physics 13 (2011) 4853.
[54] M.D. Segall, P.L.D. Lindan, M.J. Probert, C.J. Pickard, P.J. Hasnip, S.J. Clark, M.C. Payne, Journal of Physics-Condensed Matter 14 (2002) 2717.
[55] J.P. Perdew, K. Burk, M. Ernzerhof, Physical Review Letters 77 (1996) 3865.
[56] J.P. Perdew, Y. Wang, Physical Review B 45 (1992) 13244.
[57] H.J. Monkhorst, J.D. Pack, Physical Review B 13 (1976) 5188.
[58] R. Long, N.J. English, Journal of Physical Chemistry C 113 (2009) 8373.
[59] C.D. Valentin, E. Finazzi, G. Pacchioni, Chemistry of Materials 20 (2008) 3706.
[60] Z.H. Xu, J.G. Yu, Nanoscale 3 (2011) 3138.
[61] J.G. Yu, Q. Li, S.W. Liu, M. Jaroniec, Chemistry-A European Journal 19 (2013) 2433.
[62] J.G. Yu, P. Zhou, Q. Li, Physical Chemistry Chemical Physics (2013), http://dx.doi.org/10.1039/C3CP44651D.
[63] X.X. Yu, J.G. Yu, B. Cheng, B.B. Huang, Chemistry-A European Journal 15 (2009) 6731.
[64] Y.N. Wang, K.J. Deng, L.Z. Zhang, Journal of Physical Chemistry C 115 (2011) 14300.